



Simulated Long-term Evolution of the Thermosphere during the Holocene: 1. Neutral Density and Temperature

Yihui Cai^{1,2,3}, Xinan Yue^{1,2,3}, Xu Zhou^{1,3}, Zhipeng Ren^{1,2,3}, Yong Wei^{1,2,3}, Yongxin Pan^{1,2,3}

¹Key Laboratory of Earth and Planetary Physics, Institute of Geology and Geophysics, Chinese Academy of Sciences, Beijing, 100029, China

²College of Earth and Planetary Sciences, University of Chinese Academy of Sciences, Beijing, 100029, China

³Beijing National Observatory of Space Environment, Institute of Geology and Geophysics, Chinese Academy of Sciences, Beijing, 100029, China

Correspondence to: Xinan Yue (yuexinan@mail.iggcas.ac.cn)

Abstract. In the previous work of Yue et al. (2022), the ionospheric evolution during the Holocene (9455 BC to 2015 AD) was comprehensively and carefully investigated for the first time using the Global Coupled Ionosphere-Thermosphere-Electrodynamics Model developed at the Institute of Geology and Geophysics, Chinese Academy of Sciences (GCITEM-IGGCAS), driven by realistic geomagnetic fields, CO₂ levels, and solar activity derived from the ancient media records and modern measurements. In this study, we further quantify the effects of the three drivers on thermospheric neutral density and temperature variations during the Holocene. We find that the oscillations of solar activity contribute more than 80% of the thermospheric variability, while either CO₂ or the geomagnetic field contributes less than 10%. The effect of CO₂ on the global mean neutral density and temperature is comparable to that of the geomagnetic field throughout the Holocene but is more significant after 1800 AD. In addition, thermospheric density and temperature show approximately linear variations with the dipole moment of the geomagnetic field, CO₂, and F10.7, with only the linear growth rate associated with the geomagnetic field varying significantly in universal time and latitude. The increasing dipole moment and CO₂ cool and contract the thermosphere, while solar activity has the opposite effect. The higher the altitude, the greater the influence of the three factors on the thermosphere. Different factors produce different seasonal variations in thermosphere changes. Furthermore, we predict that a 400 ppm increase in CO₂ will result in a 50–70% and 84–114 K reduction in global mean neutral density and temperature, respectively, which should directly affect the orbit and lifetime of spacecraft and space debris.

1 Introduction

Global glaciers have been melting in the recent century due to climate warming, and this melting has been accelerating in the last 20 years, leading to rising sea levels and elevating natural disasters (Hugonnet et al., 2021; Zemp et al., 2019). The main cause of climate warming is the use of fossil fuels as a source of anthropogenic greenhouse gases (Tollefson, 2021). The simulations of Roble and Dickinson (1989) show that the increase in greenhouse gases warms the troposphere, but cools the thermosphere. The long-term trend studies in subsequent decades largely support this consensus (Laštovička, 2009; Laštovička et al., 2006; Laštovička et al., 2008). Tropospheric warming seriously affects human life, while changes in the thermosphere

affect various human-launched satellites, space stations, and spacecraft, such as the SpaceX Starlink satellites destruction event on 4 February 2022 (Dang et al., 2022; Lin et al., 2022), therefore is also relevant to human life. The current understanding of the thermosphere is based on modern satellite observations over the last ~70 years. The energy sources driving the variability of the thermosphere include mainly solar irradiance and geomagnetic activity generated by the interaction between the solar wind and the Earth's magnetic field (Knipp et al., 2004). These two energy sources are responsible for thermospheric temporal variations on time scales ranging from minutes to decades. On longer time scales, however, the effects of greenhouse gases and the geomagnetic field must be taken into account (Laštovička et al., 2006). Several review papers have summarized the knowledge of thermospheric variations and their driving mechanisms (Laštovička, 2017; Laštovička et al., 2012; Qian et al., 2011; Qian & Solomon, 2012).

Long-term trends of neutral density at different altitudes between 200 and 600 km have been extensively investigated using satellite orbit measurements since the 1960s (Emmert, 2015; Emmert et al., 2004; Emmert et al., 2008; Keating et al., 2000; Marcos et al., 2005; Saunders et al., 2011). These studies suggested that the trend is mainly attributed to a dramatic increase in anthropogenic greenhouse gases and becomes stronger with increasing altitude. A summary of the trends derived from satellite orbit data can be found in Emmert (2015) and Solomon et al. (2018). Overall, the observed long-term trend of the thermospheric neutral density at 400 km ranges from -2% to -5% per decade. These observed characteristics are qualitatively consistent with the model-predicted effects of increasing CO₂ concentrations. (Qian et al., 2006; Roble & Dickinson, 1989; Solomon et al., 2015). The effect of geomagnetic field strength and configuration on the thermosphere has also been paid enormous attention from observations and simulations (A et al., 2012; Cnossen, 2014; Cnossen, 2022; Cnossen & Maute, 2020; Cnossen et al., 2012; Cnossen et al., 2011; Förster & Cnossen, 2013). However, none of these effects are as significant as the effect of solar activity on the thermosphere. The amplitude of the solar-driven variation increases with height, by a factor of two for temperature and an order of magnitude for density in the upper thermosphere (Qian & Solomon, 2012; Solomon et al., 2019). Overall, these observations and simulations of the thermosphere are limited to the recent 100 years, while the "ancient" thermosphere has never been investigated on longer time scales such as during the Holocene. Therefore, we propose to reconstruct the paleo-thermosphere since the Holocene using the first principle numerical model driven by these indices including solar activity derived from tree ring (Solanki et al., 2004), paleo geomagnetic field model (Korte et al., 2011), and greenhouse gas concentration derived from polar ice core (Lüthi et al., 2008). Based on the reconstructed simulations, we can understand in detail the evolution of the thermosphere over 10,000 years and the effects of changes in the geomagnetic field, CO₂, and solar activity on the thermosphere, which can provide a foundation for the future effect of climate change on human life.

The rest of the paper is organized as follows. Section 2 will briefly describe the numerical model and driving parameters used in this study. Section 3 will show the simulation results and discuss them. Finally, we draw conclusions in Section 4.



2 Methodology

This study will use the Global Coupled Ionosphere-Thermosphere-Electrodynamics Model developed at the Institute of Geology and Geophysics, Chinese Academy of Sciences (GCITEM-IGGCAS) (Ren et al., 2009), which is the same as Yue et al. (2022). This model self-consistently solves the energy, momentum, and continuity equations of neutrals and ions in altitude coordinate rather than pressure level coordinate between 90 and 600 km, and solves the electrodynamic equations using magnetic apex coordinate (Richmond, 1995) based on provided spherical harmonic coefficients of any dipole-dominated geomagnetic field, such as the International Geomagnetic Reference Field (IGRF) model (Alken et al., 2021). This model has a good performance that has been confirmed by several ionospheric and thermospheric weather and climate simulations (Ren et al., 2011; Ren et al., 2020; Ren et al., 2010; Yue et al., 2022; Zhou et al., 2022). To remove the effects of initial conditions, each simulation is run for an interval of 15 days, and the final day results are used for further analysis.

Three drivers associated with geomagnetic field, CO₂ level, and solar activity during the Holocene, 9455 BC to 2015 AD, are used to drive the GCITEM-IGGCAS. These drivers have been summarized in Figure 1 of Yue et al. (2022). The geomagnetic field is CALS10k.2 (Constable et al., 2016) for the period 9455 BC to 1900 AD and IGRF after 1990. The geomagnetic field has undergone complex and nonlinear changes during the Holocene, with a dipole moment variation of ~40%, much larger than the ~7% variation since 1900. The CO₂ concentration evolution that is derived from Antarctica Vostok and EPICA Dome C ice cores (Lüthi et al., 2008), Antarctica Law Dome ice cores (Macfarling Meure et al., 2006), and direct atmospheric measurement at Mauna Loa Observatory, Hawaii (Keeling et al., 1995). The CO₂ concentration increases roughly linearly from 250 ppm (parts per million) around 10,000 BC to 402 ppm around 2015 AD, with a major increase occurring after 1800. The F10.7 index evolution converted from the tree ring derived sunspot number (SSN) (Solanki et al., 2004) and the group SSN (Hoyt & Schatten, 1998), and modern instrument measurement (Tapping, 2013), which reveals the long-term oscillations in solar activity with relatively high solar activity around 9000 BC and 1960 AD. A detailed description of the three drivers can be found in Yue et al. (2022).

In this simulation, four control runs (CR1–CR4) have been implemented, which is the same as Yue et al. (2022) (summarized in their Table 1). CR1 is used to identify the effect of geomagnetic field variation on thermospheric evolution. CR2 is used to reveal the effect of CO₂. CR3 is used to diagnose the combined effect of geomagnetic field and CO₂. CR4 is used to determine the combined effects of geomagnetic field variation, solar activity, and CO₂. In addition, the combined analysis of the simulations of CR3 and CR4 allows for discerning the effect of solar activity.

3 Results and Discussions

3.1 Thermosphere evolution during Holocene

Figure 1 shows the overall evolution of the CR4 simulated thermospheric neutral density and temperature in the March equinox during the Holocene. The top row displays the time evolution of the global mean neutral density and temperature at 400 km,



and the other rows give the global map of neutral density and temperature at 400 km at Universal Time (UT) 19:00 for the
95 considered four years (9005 BC, 7635 BC, 3015 BC, and 2005 AD). The white text of the global map in the left column of
Figure 1 gives the corresponding F10.7 index, CO₂ level, and dipole moment of the geomagnetic field. It is clear that the global
mean neutral density and temperature are mainly controlled by solar activity as they show essentially the same temporal
evolution and oscillation as solar activity. The higher the solar activity, the larger the neutral density and temperature in general,
with a relatively larger value around 9000 BC and 1960 AD. The global distribution of neutral density and temperature shows
100 a remarkable feature during the dayside with two peaks on either side of the geomagnetic inclination equator, so-called
equatorial mass anomaly (EMA), like the equatorial ionization anomaly (EIA) in the ionosphere (Appleton, 1946; Balan et al.,
2018), indicating a strong coupling between the thermosphere and ionosphere modulated by the geomagnetic field at low and
middle latitudes (Hedin & Mayr, 1973; H. Liu et al., 2005; Huixin Liu et al., 2007; Raghavarao et al., 1993; Raghavarao et al.,
1991). Comparing the simulations for the considered four years can basically reveal the influence of CO₂, geomagnetic field,
105 and solar activity on the evolution of the thermosphere. The F10.7 index and CO₂ level used to drive GCITEM-IGGCAS are
similar in 9005 BC and 7635 BC, except that the dipole moment is about 20% larger in 7635 BC than in 9005 BC. It is clear
that the simulated neutral density and temperature for these two years are not significantly different in global distribution
pattern and magnitude, which indicates that the ~20% change in dipole moment has a weak effect on the thermosphere at 400
km altitude. Comparing the simulations of 9005 BC and 3015 BC reveals that a ~25% reduction of the F10.7 index leads to a
110 ~50% decrease in neutral density and a ~170 K decrease in neutral temperature. Furthermore, the cooling effect of CO₂ on the
thermosphere can be found by comparing the simulations of 9005 BC and 2005 AD. An increase of 110 ppm (~40%) of CO₂
concentration causes a temperature reduction of ~40 K and a density reduction of ~21%. In addition, we also checked the
simulations at other UTs and during the June solstice as well. In summary, the thermosphere is primarily controlled by solar
activity, with secondary controlled factors being CO₂ and geomagnetic field.

115 Figure 2 shows the global mean for all UTs and grids of the neutral density and temperature as a function of altitude and year
(left column) and the zonal mean neutral density and temperature versus latitude and year at 400 km (right column) in March
equinox during the Holocene. According to (Afraimovich et al., 2008), a latitude-dependent area weighting factor was used in
the calculation of the global mean to make it more representative. As shown in Figure 2, both the global mean and zonal mean
display significant oscillations throughout the whole Holocene, which is consistent with the oscillations of the solar activity
120 whose relative change was marked by the red lines in the left column. When F10.7 reaches its relatively higher value before
8000 BC and in the recent century, a larger value of neutral density and temperature also appear. This feature is not clear in
the altitude profile of the global mean of neutral density (top left panel) due to the span of about 10 orders of magnitude.
However, this does not affect the conclusion, after all, the fixed height of the zonal mean is more revealing of this feature.
Furthermore, the thermospheric neutral density and temperature also show significant long-term decreases from 6000 BC to
125 3500 BC and the most famous grand solar minimum (Usoskin et al., 2007), the Maunder Minimum between 1645 and 1715
(Eddy, 1976). Only a weak latitudinal variation can be seen in the zonal mean neutral temperature in the March equinox.



3.2 The effects of the three drivers on the evolution of thermospheric neutral density and temperature

In this section, the changes in thermospheric neutral density and temperature caused by the geomagnetic field, CO₂, and solar activity will be diagnosed by subtracting the beginning year (9455 BC) of the simulations, as shown in Figures 3–5 for the results of the global mean and zonal mean.

Figure 3 shows the global mean neutral density profile variations in percentage caused by the three drivers in the left column. The black, magenta, and red lines represent the relative changes of the dipole moment, CO₂, and F10.7 index, respectively, during the Holocene. In general, the higher altitude, the larger the effect of the three drivers on the neutral density, because the neutral density decreases exponentially with altitude causing all effects to be amplified at higher altitudes. For the effect of the geomagnetic field, its nonlinear variation causes a nonlinear change in the neutral density, and a decrease in its intensity represented by the weakening of the dipole moment (around 5500 BC) generally leads to an increase in the neutral density. In addition, an increase in the dipole moment would make the neutral density increase weaker, which might be related to the decrease in Joule heating due to the strong dipole moment (Cnossen et al., 2012; Cnossen et al., 2011; Glassmeier et al., 2004; Wang et al., 2017). When the dipole moment increases beyond $\sim 3 \times 10^{22}$ Am² (in ~ 7500 BC and from ~ 1500 BC to ~ 1000 AD), the density will decrease in turn between 150 and 250 km. For the effect of CO₂, the neutral density decreases during the increase phase of CO₂ level (before ~ 8000 BC and after ~ 4000 BC). This is because greenhouse gases can cool and contract the thermosphere (Qian et al., 2011), as shown in Figure 4 for temperature reduction. In turn, when CO₂ decreases between ~ 8000 BC and ~ 4000 BC, the thermosphere neutral density increases. It is worth noting that the effect of CO₂ has been more significant since 1800 AD due to the much larger growth rate of CO₂. For the effect of solar activity, the overall change in neutral density due to solar activity is more than 10 times larger than that of CO₂ and the geomagnetic field, so it is the dominant factor in neutral density change. The neutral density has increased by more than 100% in the recent century and around 9000 BC, which corresponds to relatively greater solar activity. The right column of Figure 3 is the zonal mean results at 400 km. The grey lines in panel (d) mark the latitude of the north and south magnetic poles for the corresponding year. The effects of the three drivers on the temporal evolution of the neutral density at all latitudes are similar to those characterized in the left column, with no significant latitude variations in the effects of CO₂ and solar activity, and a weak latitude variation in the effect of the geomagnetic field, which is stronger at high latitudes. The region with greater geomagnetic field effects corresponds exactly to the magnetic pole locations, such as the south magnetic pole at $\sim 64^\circ$ around 5500 BC, implying the importance of the magnetic pole locations and further supporting the contribution of Joule heating in the polar region.

Figure 4 shows a similar pattern as Figure 3 except that the neutral temperature variations are shown. Overall, the effects of CO₂ and solar activity on temperature are essentially the same as those on neutral density, only the temperature change is more significant. The dramatic increase in CO₂ level in the past century has led to a decrease in global mean neutral temperature of more than 20 K, which is well in line with previous understanding (Cnossen, 2014; Roble & Dickinson, 1989). In addition, the global mean neutral temperature increases within 5 K due to CO₂ reduction between 8000 and 4000 BC. Solar activity remains the dominant factor in the neutral temperature variability, which leads to neutral temperature changes in the range of



160 ± 200 K with its own oscillations. Furthermore, the effect of the geomagnetic field on neutral temperature differs significantly
from the effect on neutral density, but can still be explained by the geomagnetic field structure, dipole moment strength, and
Joule heating. The zonal mean temperature changes contributed by the geomagnetic field show a clear latitude variation. The
neutral temperature increases ~ 24 K at south latitude $\sim 65^\circ$ around 5500 BC, caused by a reduction in the dipole moment
resulting in stronger Joule heating around the south magnetic pole. Conversely, between 1500 BC and 1000 AD, the neutral
165 temperature in the polar regions dropped by up to 22 K due to the weakening of Joule heating caused by the increase of the
dipole moment. In addition, the effect of the geomagnetic field is significantly weaker at north latitude $\sim 10^\circ$, perhaps owing
to tides in the lower atmosphere. Although the neutral temperature changes in the polar regions are large, the change in global
mean neutral temperature due to the geomagnetic field is essentially within ± 10 K at all altitudes during Holocene. The June
simulations have also been carefully analyzed (not shown here), and the effects of CO_2 and solar activity are similar to those
170 of March, and the geomagnetic field effects differ greatly from those of March, which lead to a weakening of both the neutral
density and temperature except for an increase near 5500 BC. The contributions of geomagnetic field structure, dipole moment,
and Joule heating are still evident in the June results.

Figure 5 shows the effect of the three drivers on the global mean neutral density and temperature at 400 km, characterized by
the deviation obtained by subtracting the simulation results of the starting year. The grey dots represent the results for each
175 UT. Three main features can be extracted from Figure 5. (1) The oscillation range of neutral density at 400 km due to the
geomagnetic field, CO_2 , and solar activity variations is $[-5, 10]$, $[-60, 5]$, and $[-200, 400] \times 10^{-14} \text{ kg m}^{-3}$, respectively. While it
is $[-10, 10]$, $[-40, 5]$, and $[-200, 200]$ K for the neutral temperature. It is clear that the effect of solar activity variations is
dozens of times greater than that of CO_2 and geomagnetic field variations. (2) Both the neutral density and temperature decrease
with increasing CO_2 . (3) The effects of CO_2 and solar activity have no universal time variation, while the effects of the
180 geomagnetic field have significant universal time variation modulated by the dipole moment.

3.3 The long-term trends generated by the variations of the geomagnetic field, CO_2 , and solar activity

From Figures 3–5, it can be found that the effects of the three factors vary approximately linearly. Therefore, we calculated
linear growth rates for the effects of the three factors on neutral density and temperature, as shown in the text of each panel in
Figure 6, which reveals the long-term trends of the thermosphere generated by the variations of the geomagnetic field (dipole
185 moment and the colatitude of the north magnetic pole), CO_2 , and solar activity, respectively. The grey dots in Figure 6 are the
global mean value of neutral density (left column) and temperature (right column) at 400 km in the March equinox of the
corresponding year in the simulations driven by the three drivers. The red lines are the result of the least squares fitting. The
neutral density and temperature show a significant linear variation with the three drivers, while the nonlinear effect of the
geomagnetic field can be found in the first and second rows, shown by the scattered grey dots on both sides of the red line.
190 Although the fitted density is generally smaller when F10.7 is greater than 110 in the bottom left panel, the linear variation of
the simulated neutral density with F10.7 is still clearly visible, only presenting a larger linear growth rate. The average value



of the global mean neutral density at 400 km over the entire simulation time interval is about $2.26 \times 10^{-12} \text{ kg m}^{-3}$. Based on this value and the linear growth rate shown in Figure 6, the effects due to changes in the geomagnetic dipole moment, the colatitude of north magnetic pole, CO_2 , and solar activity during the entire Holocene can be calculated to be about -1.4% , -1.6% , -31% and $+250\%$, respectively. While the effects are about -7 K , -4 K , -48 K , and $+557 \text{ K}$ for the neutral temperature, respectively. Solomon et al. (2019) pointed out that the temperature change from solar minimum to maximum increases by about 500 K at 400 km based on the simulation of the Whole Atmosphere Community Climate Model-eXtended (WACCM-X), which is generally consistent with our results. Since the effect of magnetic pole position is not as large as that of dipole moment, only the dipole moment is used later to quantify the effect of the magnetic field.

Figure 7 shows the altitude variations of the linear growth rate (dashed lines) and the corresponding change in percentage (solid lines) of the global mean neutral density (left column) and temperature (right column) resulting from the three drivers in the March equinox (black lines) and June solstice (red lines). The effect of the three drivers on the neutral temperatures of March and June essentially increases with altitude, but it is close to constant above 300 km. The effect of the geomagnetic field on the neutral temperature is slightly greater in June than in March. For every 10^{22} Am^2 increase in dipole moment, the neutral temperature in June decreases by $\sim 2.7 \text{ K}$, compared to $\sim 1.7 \text{ K}$ in March. In contrast, CO_2 and solar activity have the opposite effect on neutral temperature, with a greater effect in March. For every 10 ppm increase in CO_2 , the global mean neutral temperature above 200 km decreases by $\sim 3.5 \text{ K}$ in March and $\sim 2.3 \text{ K}$ in June. Akmaev and Fomichev (1998) suggested a trend of about -3.1 K per 10 ppm at 200 km in the thermosphere in April due to increasing CO_2 , while Cnossen (2014) and Solomon et al. (2018) reported trends of about -1 K and -1.8 K per 10 ppm above 200 km, respectively. Therefore, it is reasonable that our results are $0.8\text{--}3.5 \text{ K}$ per 10 ppm between 150 and 600 km. For each 1 sfu increase in F10.7, the neutral temperature increase is $\sim 6.2 \text{ K}$ and $\sim 4.4 \text{ K}$ in March and June, respectively. The effect of the three factors on neutral density is similar to that on neutral temperature. Since neutral density decreases exponentially with altitude, the effect of the three factors on neutral density (absolute value change) also decreases with an altitude above 150 km, as shown in the left column of Figure 7. To present more clearly the effect of the three factors on neutral density, the solid lines display the corresponding percentage changes using 2005 simulations of CR4 as a reference. This reveals that the effects of solar activity and dipole moment on neutral density increase significantly with increasing altitude in March and June with a stronger effect in June, while the effect of CO_2 is basically unchanged with altitude in both March and June with a stronger effect in March. In addition, the increasing dipole moment and CO_2 decrease the neutral density, while the rising solar activity increases the neutral density.

As mentioned in Section 3.2, only the effect of the geomagnetic field on the thermosphere displays the latitude and UT variations. Figure 8 shows the linear growth rate of neutral density (top row) and temperature (bottom row) at 400 km attributed to the geomagnetic field versus latitude and UT (left column) or longitude (right column). In general, an increase in the dipole moment attenuates the thermospheric neutral density and temperature at all latitudes, longitudes, and UTs. The linear growth rate is greater at high latitudes in the 0–8 and 18–24 UT and can reach $-3.6 \times 10^{-14} \text{ kg m}^{-3}/10^{22} \text{ Am}^2$ or $-9.5 \text{ K}/10^{22} \text{ Am}^2$, while it is about $-1 \times 10^{-14} \text{ kg m}^{-3}/10^{22} \text{ Am}^2$ or $-2 \text{ K}/10^{22} \text{ Am}^2$ at other latitudes and UTs. In addition, a larger linear growth rate of



225 up to $-4.4 \times 10^{-14} \text{ kg m}^{-3}/10^{22} \text{ Am}^2$ or $-8.7 \text{ K}/10^{22} \text{ Am}^2$ is seen in all longitudes above $\pm 60^\circ$ latitude, and it is also about $-1 \times 10^{-14} \text{ kg m}^{-3}/10^{22} \text{ Am}^2$ or $-2 \text{ K}/10^{22} \text{ Am}^2$ in other regions. Overall, the thermosphere in the polar regions of the Southern Hemisphere is more influenced by the geomagnetic field than that in the Northern Hemisphere, while the influence of the magnetic field is weaker and of about a similar magnitude in the middle and low latitudes.

3.4 Future projections

230 As the number of human space missions increases explosively, more and more spacecraft will operate in the thermosphere, so projecting the future state of the thermosphere is also important to human life. Based on the IPCC projections of greenhouse gas emissions under different scenarios (IPCC, 2014), we can simply and reasonably assume that CO_2 concentrations will rise by 400 ppm over the next century. Therefore, according to the calculations shown in Table 2, the global mean neutral density will decrease by $\sim 70\%$ and $\sim 50\%$ in March and June, respectively, due to a 400 ppm increase in CO_2 . This is generally
235 consistent with the trend of about $-6.1 \pm 0.8\%$ per decade throughout the 21st century projected by Cnossen (2022). Also, from Figure 7, it can be concluded that the neutral temperatures in March and June will decrease by $\sim 114 \text{ K}$ and $\sim 84 \text{ K}$, respectively. This is larger than the projections ($\sim 60 \text{ K}$) of Cnossen (2022).

The dipole moment decreases by about 3.5% over the next 50 years based on the prediction by Aubert (2015), causing an increase in global mean neutral density of up to 1% above 500 km according to the simulations of Cnossen and Maute (2020).
240 However, the increase of the global mean neutral density is projected to be $\sim 0.08\%$ and $\sim 0.25\%$ in March and June, respectively, based on our calculated linear growth rate. In addition, we can also project that the temperature increase due to the decrease of dipole moment in March and June is about 0.5 K and 0.7 K, respectively. As shown in Figure 8, the effect of the geomagnetic field is strongly dependent on UT and geographic location, so the global mean state projection is provided for reference only. Furthermore, the effect of geomagnetic field variation is negligible compared to the effect of rising CO_2 over the next 100
245 years.

4 Conclusions

In this study, the evolution of the thermosphere during the Holocene (from 9455 BC to 2015 AD) was simulated using the independently developed global ionosphere-thermosphere theoretical model GCITEM-IGGCAS, driven by the realistic geomagnetic field model, CO_2 level, and solar activity derived from modern measurements and ancient natural media.
250 Furthermore, through a series of control simulations, we quantify the thermospheric temperature and density changes due to variations in the geomagnetic field, CO_2 levels, and solar activity. The main conclusions are presented below.

1. The climatological morphology of the global thermosphere during the Holocene is reconstructed for the first time. Thermospheric neutral density is mainly controlled by solar activity and modulated by CO_2 and geomagnetic field. Typically, the geomagnetic field configuration directly affects the morphology of the equatorial mass anomaly structure
255 of the thermosphere, while CO_2 mainly affects the magnitude of the neutral density and temperature. In general, the



260 frequent oscillations of solar activity contribute more than 80% of the thermospheric variability, while the contributions of CO₂ and geomagnetic field are both less than 10%. The effect of CO₂ is comparable to that of the geomagnetic field throughout the Holocene for the global mean neutral density and temperature but becomes more significant after 1800 AD. Only the effect of the geomagnetic field is strongly dependent on the universal time and geographical location, and the weakening of the dipole moment leading to an increase in Joule heating in the polar region thus make the thermosphere change more than the effect of CO₂. Overall, the higher altitude, the larger the effect of the three drivers on the neutral density and temperature.

- 265 2. Both the thermospheric neutral density and temperature vary approximately linearly with the dipole moment of the geomagnetic field, CO₂, and the F10.7 index of solar activity. The global mean variability of the neutral density at 400 km during the March equinox due to changes in the geomagnetic dipole moment, CO₂, and solar activity during the entire Holocene can be about -1.4%, -31%, and +250%, respectively. While the effects are about -7 K, -48 K, and +557 K for the neutral temperature, respectively. In addition, there is a clear altitude and seasonal variation in the thermosphere change due to an increase in per unit of dipole moment, CO₂, and solar activity. Different factors produce different seasonal variations in thermosphere changes. The increasing dipole moment and CO₂ decrease the neutral density and 270 temperature, while the rising solar activity increases them.
3. We project that a 400 ppm increase in CO₂ will result in a 50–70% reduction in global mean thermospheric neutral density depending on the season, while neutral temperatures will decrease by 84–114 K. This is enough to change the orbit and lifetime of spacecraft and space debris, which deserves the attention of future space missions. The effect of decreasing dipole moments of the geomagnetic field over the next 100 years on the global mean thermospheric neutral density and 275 temperature is negligible, but the effect of changing magnetic field configurations (e.g., magnetic pole positions) on the thermosphere should be considered, especially in the polar regions.

Data availability

The spherical harmonic coefficients of CALS10k.2 model was obtained from the website: <https://earthref.org/ERDA/2207>. The IGRF model was downloaded from the website: <https://www.ngdc.noaa.gov/IAGA/vmod/igrf.html>. The Antarctica Vostok and EPICA Dome C ice cores CO₂ level was derived from the website: <https://data.noaa.gov/dataset/dataset/noaa-wds-paleoclimatology-aicc2012-800kyr-antarctic-ice-core-chronology>. The Antarctica Law Dome ice core CO₂ data was downloaded from the website: <https://www.ncei.noaa.gov/access/metadata/landing-page/bin/iso?id=noaa-icecore-9959>. The Mauna Loa observed CO₂ was from the website: <https://gml.noaa.gov/ccgg/trends/data.html>. The 11,000 yr reconstructed sunspot number was downloaded from the NOAA website: https://www.ncei.noaa.gov/pub/data/paleo/climate_forcing/solar_variability/solanki2004-ssn.txt. The group sunspot number was downloaded from the NGDC website: <https://ngdc.noaa.gov/stp/solar/ssndata.html>. The modern F10.7 index was from



<http://spidr.ngdc.noaa.gov/>. The simulated data by the GCITEM-IGGCAS model under different control runs are available at:
<http://doi.org/10.17605/OSF.IO/ZQ8HY>.

Competing interests

290 The contact author has declared that neither of the authors has any competing interests.

Acknowledgements

The authors acknowledge the support of the B-type Strategic Priority Program of the Chinese Academy of Sciences (Grant XDB41000000), the Project of Stable Support for Youth Team in Basic Research Field, CAS (YSBR-018), the National Natural Science Foundation of China (41621004, 42241106, 42204165), the CAS Youth Interdisciplinary Team (JCTD-2021-
295 05), and the Key Research Program of the Institute of Geology and Geophysics, CAS (Grant IGGCAS-201904).

References

- A, E., Ridley, A. J., Zhang, D., & Xiao, Z. (2012). Analyzing the hemispheric asymmetry in the thermospheric density response to geomagnetic storms. *Journal of Geophysical Research: Space Physics*, 117(A8), A08317. <https://doi.org/10.1029/2011ja017259>
- 300 Afraimovich, E. L., Astafyeva, E. I., Oinats, A. V., Yasukevich, Y. V., & Zhivetiev, I. V. (2008). Global electron content: a new conception to track solar activity. *Annales Geophysicae*, 26(2), 335-344. <https://doi.org/10.5194/angeo-26-335-2008>
- Akmaev, R. A., & Fomichev, V. I. (1998). Cooling of the mesosphere and lower thermosphere due to doubling of CO₂. *Annales Geophysicae*, 16(11), 1501-1512. <https://doi.org/10.1007/s00585-998-1501-z>
- 305 Alken, P., Thébaud, E., Beggan, C. D., Amit, H., Aubert, J., Baerenzung, J., et al. (2021). International Geomagnetic Reference Field: the thirteenth generation. *Earth, Planets and Space*, 73(1), 49. <https://doi.org/10.1186/s40623-020-01288-x>
- Appleton, E. V. (1946). Two Anomalies in the Ionosphere. *Nature*, 157(3995), 691-691. <https://doi.org/10.1038/157691a0>
- Aubert, J. (2015). Geomagnetic forecasts driven by thermal wind dynamics in the Earth's core. *Geophysical Journal International*, 203(3), 1738-1751. <https://doi.org/10.1093/gji/ggv394>
- 310 Balan, N., Liu, L., & Le, H. (2018). A brief review of equatorial ionization anomaly and ionospheric irregularities. *Earth and Planetary Physics*, 2(4), 257-275. <https://doi.org/10.26464/epp2018025>
- Cnossen, I. (2014). The importance of geomagnetic field changes versus rising CO₂ levels for long-term change in the upper atmosphere. *J. Space Weather Space Clim.*, 4, A18. <https://doi.org/10.1051/swsc/2014016>
- Cnossen, I. (2022). A Realistic Projection of Climate Change in the Upper Atmosphere Into the 21st Century. *Geophysical Research Letters*, 49(19), e2022GL100693. <https://doi.org/10.1029/2022gl100693>
- 315 Cnossen, I., & Maute, A. (2020). Simulated Trends in Ionosphere-Thermosphere Climate Due to Predicted Main Magnetic Field Changes From 2015 to 2065. *Journal of Geophysical Research: Space Physics*, 125(3), e2019JA027738. <https://doi.org/10.1029/2019ja027738>



- 320 Cnossen, I., Richmond, A. D., & Wiltberger, M. (2012). The dependence of the coupled magnetosphere-ionosphere-thermosphere system on the Earth's magnetic dipole moment. *Journal of Geophysical Research: Space Physics*, 117(A5), A05302. <https://doi.org/10.1029/2012JA017555>
- Cnossen, I., Richmond, A. D., Wiltberger, M., Wang, W., & Schmitt, P. (2011). The response of the coupled magnetosphere-ionosphere-thermosphere system to a 25% reduction in the dipole moment of the Earth's magnetic field. *Journal of Geophysical Research: Space Physics*, 116(A12), A12304. <https://doi.org/10.1029/2011ja017063>
- 325 Constable, C., Korte, M., & Panovska, S. (2016). Persistent high paleosecular variation activity in southern hemisphere for at least 10 000 years. *Earth and Planetary Science Letters*, 453, 78-86. <https://doi.org/10.1016/j.epsl.2016.08.015>
- Dang, T., Li, X., Luo, B., Li, R., Zhang, B., Pham, K., et al. (2022). Unveiling the Space Weather During the Starlink Satellites Destruction Event on 4 February 2022. *Space Weather*, 20(8), e2022SW003152. <https://doi.org/10.1029/2022sw003152>
- 330 Eddy, J. A. (1976). The Maunder Minimum. *Science*, 192(4245), 1189-1202. <https://doi.org/10.1126/science.192.4245.1189>
- Emmert, J. T. (2015). Altitude and solar activity dependence of 1967-2005 thermospheric density trends derived from orbital drag. *Journal of Geophysical Research: Space Physics*, 120(4), 2940-2950. <https://doi.org/10.1002/2015ja021047>
- Emmert, J. T., Picone, J. M., Lean, J. L., & Knowles, S. H. (2004). Global change in the thermosphere: Compelling evidence of a secular decrease in density. *Journal of Geophysical Research: Space Physics*, 109(A2), A02301. <https://doi.org/10.1029/2003ja010176>
- 335 Emmert, J. T., Picone, J. M., & Meier, R. R. (2008). Thermospheric global average density trends, 1967–2007, derived from orbits of 5000 near-Earth objects. *Geophysical Research Letters*, 35(5), L05101. <https://doi.org/10.1029/2007gl032809>
- Förster, M., & Cnossen, I. (2013). Upper atmosphere differences between northern and southern high latitudes: The role of magnetic field asymmetry. *Journal of Geophysical Research: Space Physics*, 118(9), 5951-5966. <https://doi.org/10.1002/jgra.50554>
- 340 Glassmeier, K. H., Vogt, J., Stadelmann, A., & Buchert, S. (2004). Concerning long-term geomagnetic variations and space climatology. *Annales Geophysicae*, 22(10), 3669-3677. <https://doi.org/10.5194/angeo-22-3669-2004>
- Hedin, A. E., & Mayr, H. G. (1973). Magnetic control of the near equatorial neutral thermosphere. *Journal of Geophysical Research*, 78(10), 1688-1691. <https://doi.org/10.1029/ja078i010p01688>
- 345 Hoyt, D. V., & Schatten, K. H. (1998). Group Sunspot Numbers: A New Solar Activity Reconstruction. *Solar Physics*, 179(1), 189-219. <https://doi.org/10.1023/A:1005007527816>
- Hugonnet, R., McNabb, R., Berthier, E., Menounos, B., Nuth, C., Girod, L., et al. (2021). Accelerated global glacier mass loss in the early twenty-first century. *Nature*, 592(7856), 726-731. <https://doi.org/10.1038/s41586-021-03436-z>
- 350 IPCC. (2014). *Climate Change 2014: Synthesis Report. Contribution of Working Groups I, II and III to the Fifth Assessment Report of the Intergovernmental Panel on Climate Change [Core Writing Team, R.K. Pachauri and L.A. Meyer (eds.)]. IPCC, Geneva, Switzerland, 151 pp.*
- Keating, G. M., Tolson, R. H., & Bradford, M. S. (2000). Evidence of long term global decline in the Earth's thermospheric densities apparently related to anthropogenic effects. *Geophysical Research Letters*, 27(10), 1523-1526. <https://doi.org/10.1029/2000gl003771>
- 355 Keeling, C. D., Whorf, T. P., Wahlen, M., & Van Der Plichtt, J. (1995). Interannual extremes in the rate of rise of atmospheric carbon dioxide since 1980. *Nature*, 375(6533), 666-670. <https://doi.org/10.1038/375666a0>
- Knipp, D. J., Tobiska, W. K., & Emery, B. A. (2004). Direct and Indirect Thermospheric Heating Sources for Solar Cycles 21–23. *Solar Physics*, 224(1), 495. <https://doi.org/10.1007/s11207-005-6393-4>



- 360 Korte, M., Constable, C., Donadini, F., & Holme, R. (2011). Reconstructing the Holocene geomagnetic field. *Earth and Planetary Science Letters*, 312(3-4), 497-505. <https://doi.org/10.1016/j.epsl.2011.10.031>
- Laštovička, J. (2009). Global pattern of trends in the upper atmosphere and ionosphere: Recent progress. *Journal of Atmospheric and Solar-Terrestrial Physics*, 71(14), 1514-1528. <https://doi.org/10.1016/j.jastp.2009.01.010>
- 365 Laštovička, J. (2017). A review of recent progress in trends in the upper atmosphere. *Journal of Atmospheric and Solar-Terrestrial Physics*, 163, 2-13. <https://doi.org/10.1016/j.jastp.2017.03.009>
- Laštovička, J., Akmaev, R. A., Beig, G., Bremer, J., & Emmert, J. T. (2006). Global Change in the Upper Atmosphere. *Science*, 314(5803), 1253-1254. <https://doi.org/10.1126/science.1135134>
- 370 Laštovička, J., Akmaev, R. A., Beig, G., Bremer, J., Emmert, J. T., Jacobi, C., et al. (2008). Emerging pattern of global change in the upper atmosphere and ionosphere. *Ann. Geophys.*, 26(5), 1255-1268. <https://doi.org/10.5194/angeo-26-1255-2008>
- Laštovička, J., Solomon, S. C., & Qian, L. (2012). Trends in the Neutral and Ionized Upper Atmosphere. *Space Science Reviews*, 168(1), 113-145. <https://doi.org/10.1007/s11214-011-9799-3>
- 375 Lin, D., Wang, W., Garcia-Sage, K., Yue, J., Merkin, V., McInerney, J. M., et al. (2022). Thermospheric Neutral Density Variation During the “SpaceX” Storm: Implications From Physics-Based Whole Geospace Modeling. *Space Weather*, 20(12), e2022SW003254. <https://doi.org/10.1029/2022sw003254>
- Liu, H., Lühr, H., Henize, V., & Köhler, W. (2005). Global distribution of the thermospheric total mass density derived from CHAMP. *Journal of Geophysical Research: Space Physics*, 110(A4), A04301. <https://doi.org/10.1029/2004ja010741>
- Liu, H., Lühr, H., & Watanabe, S. (2007). Climatology of the equatorial thermospheric mass density anomaly. *Journal of Geophysical Research: Space Physics*, 112(A5), A05305. <https://doi.org/10.1029/2006ja012199>
- 380 Lüthi, D., Le Floch, M., Bereiter, B., Blunier, T., Barnola, J.-M., Siegenthaler, U., et al. (2008). High-resolution carbon dioxide concentration record 650,000–800,000 years before present. *Nature*, 453(7193), 379-382. <https://doi.org/10.1038/nature06949>
- Macfarling Meure, C., Etheridge, D., Trudinger, C., Steele, P., Langenfelds, R., Van Ommen, T., et al. (2006). Law Dome CO₂, CH₄, and N₂O ice
- 385 core records extended to 2,000 yr BP. *Geophysical Research Letters*, 33(14), L14810. <https://doi.org/10.1029/2006gl026152>
- Marcos, F. A., Wise, J. O., Kendra, M. J., Grossbard, N. J., & Bowman, B. R. (2005). Detection of a long-term decrease in thermospheric neutral density. *Geophysical Research Letters*, 32(4), L04103. <https://doi.org/10.1029/2004gl021269>
- 390 Qian, L., Laštovička, J., Roble, R. G., & Solomon, S. C. (2011). Progress in observations and simulations of global change in the upper atmosphere. *Journal of Geophysical Research: Space Physics*, 116(A2), A00H03. <https://doi.org/10.1029/2010JA016317>
- Qian, L., Roble, R. G., Solomon, S. C., & Kane, T. J. (2006). Calculated and observed climate change in the thermosphere, and a prediction for solar cycle 24. *Geophysical Research Letters*, 33(23), L23705. <https://doi.org/10.1029/2006gl027185>
- 395 Qian, L., & Solomon, S. C. (2012). Thermospheric Density: An Overview of Temporal and Spatial Variations. *Space Science Reviews*, 168(1), 147-173. <https://doi.org/10.1007/s11214-011-9810-z>
- Raghavarao, R., Hoegy, W. R., Spencer, N. W., & Wharton, L. E. (1993). Neutral temperature anomaly in the equatorial thermosphere-A source of vertical winds. *Geophysical Research Letters*, 20(11), 1023-1026. <https://doi.org/10.1029/93gl01253>
- 400 Raghavarao, R., Wharton, L. E., Spencer, N. W., Mayr, H. G., & Brace, L. H. (1991). An equatorial temperature and wind anomaly (ETWA). *Geophysical Research Letters*, 18(7), 1193-1196. <https://doi.org/10.1029/91gl01561>



- Ren, Z., Wan, W., & Liu, L. (2009). GCITEM-IGGCAS: A new global coupled ionosphere–thermosphere-electrodynamics model. *Journal of Atmospheric and Solar-Terrestrial Physics*, 71(17), 2064-2076. <https://doi.org/10.1016/j.jastp.2009.09.015>
- 405 Ren, Z., Wan, W., Liu, L., & Xiong, J. (2011). Simulated longitudinal variations in the lower thermospheric nitric oxide induced by nonmigrating tides. *Journal of Geophysical Research: Space Physics*, 116(A4), A04301. <https://doi.org/10.1029/2010ja016131>
- Ren, Z., Wan, W., Xiong, J., & Li, X. (2020). A Simulation of the Influence of DE3 Tide on Nitric Oxide Infrared Cooling. *Journal of Geophysical Research: Space Physics*, 125(3), e2019JA027131. <https://doi.org/10.1029/2019ja027131>
- 410 Ren, Z., Wan, W., Xiong, J., & Liu, L. (2010). Simulated wave number 4 structure in equatorial *F*-region vertical plasma drifts. *Journal of Geophysical Research: Space Physics*, 115(A5), A05301. <https://doi.org/10.1029/2009ja014746>
- Richmond, A. D. (1995). Ionospheric Electrodynamics Using Magnetic Apex Coordinates. *Journal of geomagnetism and geoelectricity*, 47(2), 191-212. <https://doi.org/10.5636/jgg.47.191>
- 415 Roble, R. G., & Dickinson, R. E. (1989). How will changes in carbon dioxide and methane modify the mean structure of the mesosphere and thermosphere? *Geophysical Research Letters*, 16(12), 1441-1444. <https://doi.org/10.1029/GL016i012p01441>
- Saunders, A., Lewis, H., & Swinerd, G. (2011). Further evidence of long-term thermospheric density change using a new method of satellite ballistic coefficient estimation. *Journal of Geophysical Research: Space Physics*, 116(A2), A00H10. <https://doi.org/10.1029/2010ja016358>
- 420 Solanki, S. K., Usoskin, I. G., Kromer, B., Schüssler, M., & Beer, J. (2004). Unusual activity of the Sun during recent decades compared to the previous 11,000 years. *Nature*, 431(7012), 1084-1087. <https://doi.org/10.1038/nature02995>
- Solomon, S. C., Liu, H. L., Marsh, D. R., McInerney, J. M., Qian, L., & Vitt, F. M. (2018). Whole Atmosphere Simulation of Anthropogenic Climate Change. *Geophysical Research Letters*, 45(3), 1567-1576. <https://doi.org/10.1002/2017gl076950>
- 425 Solomon, S. C., Liu, H. L., Marsh, D. R., McInerney, J. M., Qian, L., & Vitt, F. M. (2019). Whole Atmosphere Climate Change: Dependence on Solar Activity. *Journal of Geophysical Research: Space Physics*, 124(5), 3799-3809. <https://doi.org/10.1029/2019ja026678>
- Solomon, S. C., Qian, L., & Roble, R. G. (2015). New 3-D simulations of climate change in the thermosphere. *Journal of Geophysical Research: Space Physics*, 120(3), 2183-2193. <https://doi.org/10.1002/2014ja020886>
- 430 Tapping, K. F. (2013). The 10.7 cm solar radio flux (F10.7). *Space Weather*, 11(7), 394-406. <https://doi.org/10.1002/swe.20064>
- Tollefson, J. (2021). IPCC climate report: Earth is warmer than it's been in 125,000 years. *Nature*, 596, 171-172. <https://doi.org/10.1038/d41586-021-02179-1>
- Usoskin, I. G., Solanki, S. K., & Kovaltsov, G. A. (2007). Grand minima and maxima of solar activity: New observational constraints. *Astron. Astrophys.*, 471(1), 301-309. <https://doi.org/10.1051/0004-6361:20077704>
- 435 Wang, H., Zhang, J., Lüher, H., & Wei, Y. (2017). Longitudinal modulation of electron and mass densities at middle and auroral latitudes: Effect of geomagnetic field strength. *Journal of Geophysical Research: Space Physics*, 122(6), 6595-6610. <https://doi.org/10.1002/2016JA023829>
- 440 Yue, X., Cai, Y., Ren, Z., Zhou, X., Wei, Y., & Pan, Y. (2022). Simulated Long-Term Evolution of the Ionosphere During the Holocene. *Journal of Geophysical Research: Space Physics*, 127(11), e2022JA031042. <https://doi.org/10.1029/2022ja031042>



Zemp, M., Huss, M., Thibert, E., Eckert, N., McNabb, R., Huber, J., et al. (2019). Global glacier mass changes and their contributions to sea-level rise from 1961 to 2016. *Nature*, 568(7752), 382-386. <https://doi.org/10.1038/s41586-019-1071-0>

445 Zhou, X., Yue, X., Ren, Z., Liu, Y., Cai, Y., Ding, F., & Wei, Y. (2022). Impact of Anthropogenic Emission Changes on the Occurrence of Equatorial Plasma Bubbles. *Geophysical Research Letters*, 49(3), e2021GL09735. <https://doi.org/10.1029/2021gl097354>



450

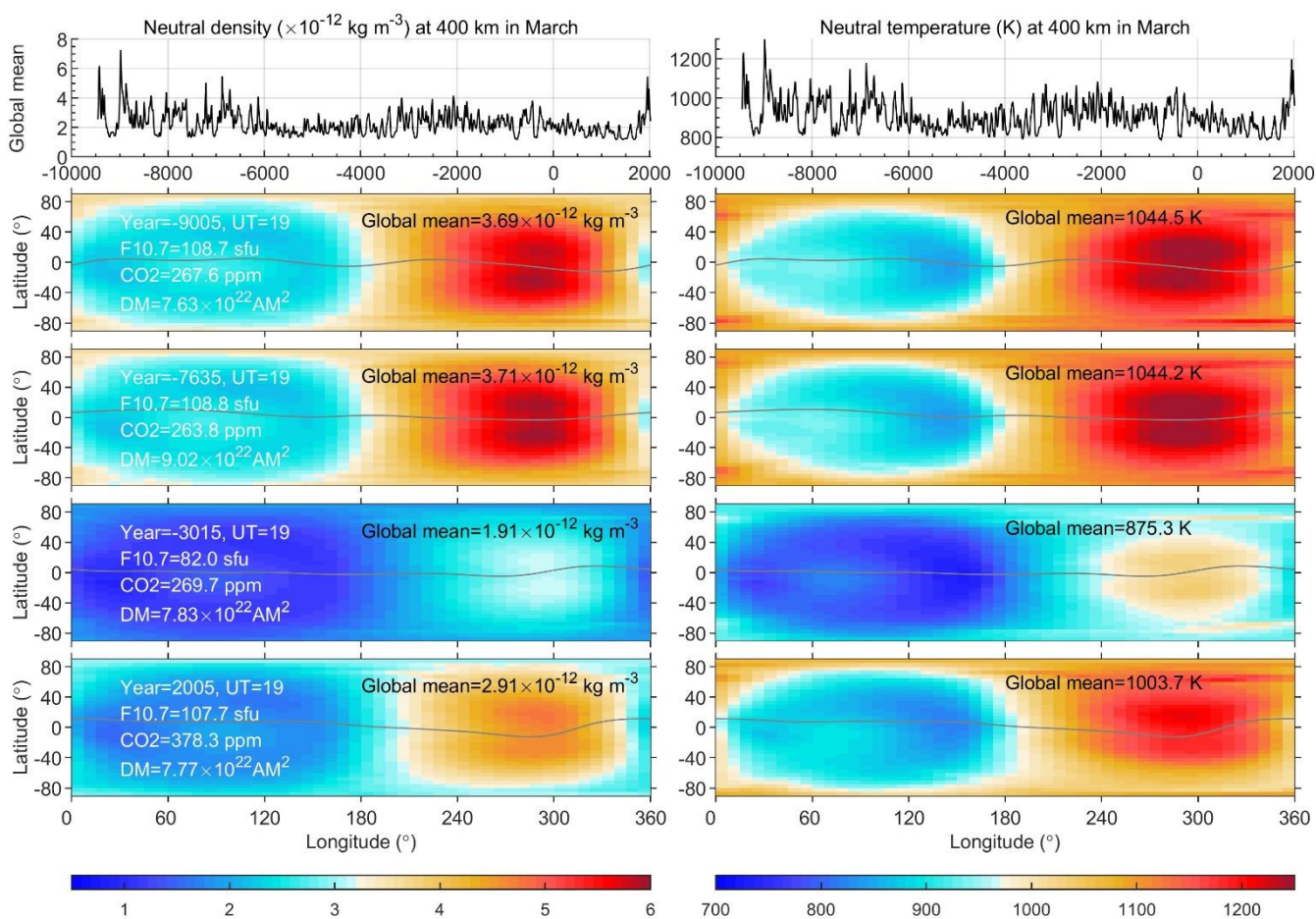


Figure 1: Time evolution of the global mean neutral density and temperature at 400 km in the March equinox (top row). The other rows are global plots of CR4 simulated neutral density (left column) and temperature (right column) for four selected years at UT 19 during the March equinox. The corresponding model drivers are also given in the white text, and ‘DM’ means the dipole moment of the geomagnetic field. The gray line in each color plot marks the inclination equator for the corresponding year.

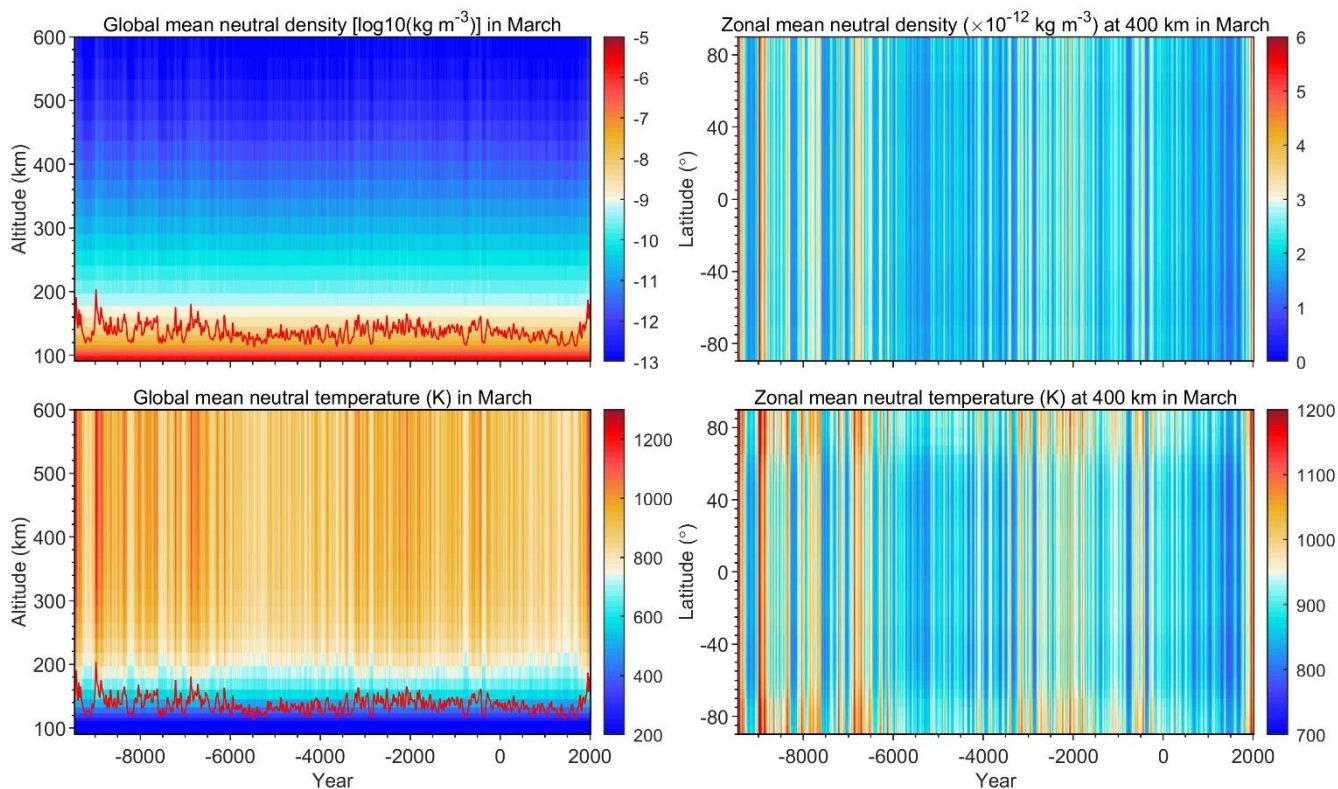


Figure 2: Global mean (all UTs and grids) neutral density and temperature profiles versus years (left column) and zonal mean (all longitudes and UTs) neutral density and temperature at 400 km as a function of latitude and years (right column) in the March equinox from CR4 simulations. Note that the color scale is different for each plot. The red line in the left column represents the relative change of the F10.7 index over the Holocene.

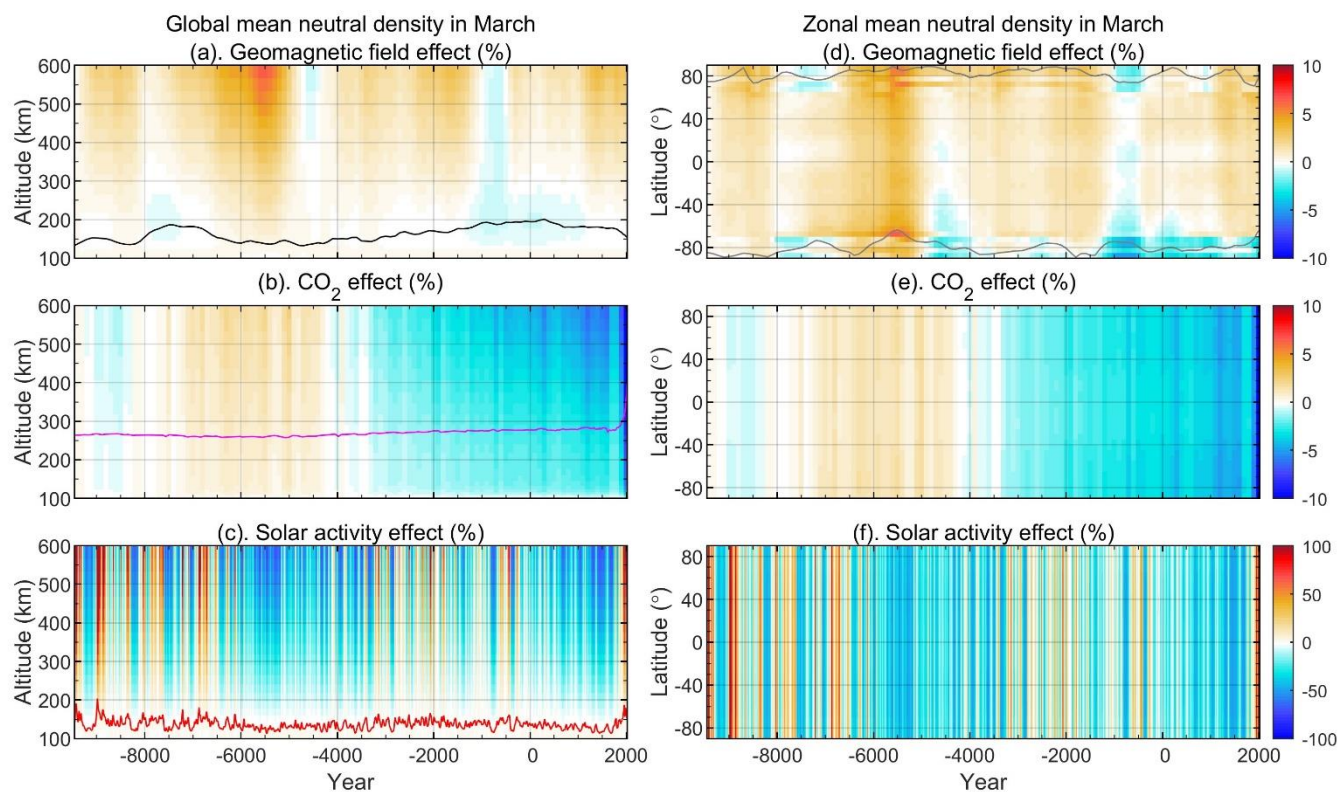
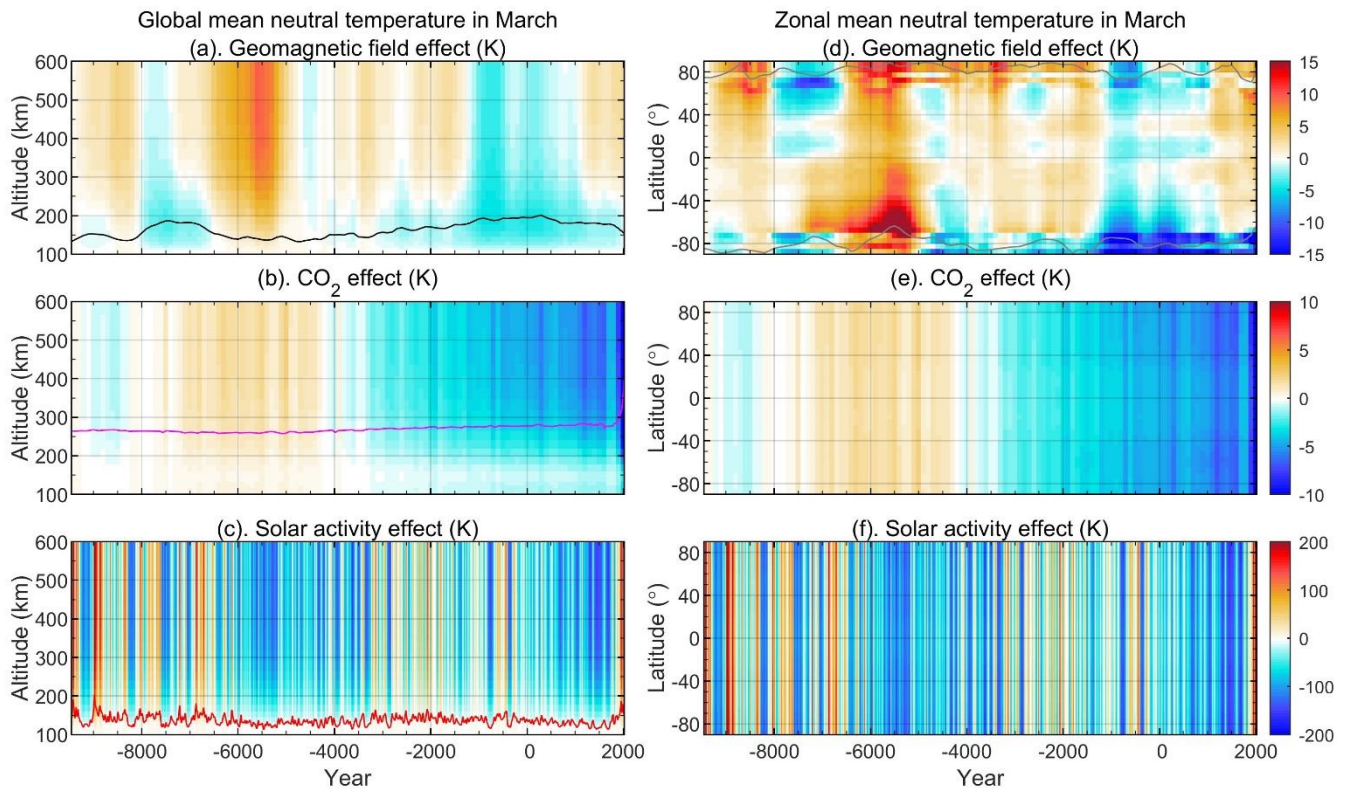


Figure 3: The global mean (all grids and UT) neutral density profiles deviate from the beginning year of the simulation due to changes in the geomagnetic field (a, CR1), CO₂ (b, CR2), and solar activity (c, CR4–CR3) as a function of altitude and 465 years. Panels (d), (e), and (f) show the same pattern as the left column except that the zonal mean neutral density (all longitudes and UTs) at 400 km is shown. The grey lines in panel (d) mark the latitude of the north and south magnetic poles for the corresponding year. The black, magenta, and red lines in the left column represent the relative changes of the dipole moment, CO₂, and F10.7 index, respectively, during the Holocene.



470

Figure 4: The same as Figure 3, but for the neutral temperature.

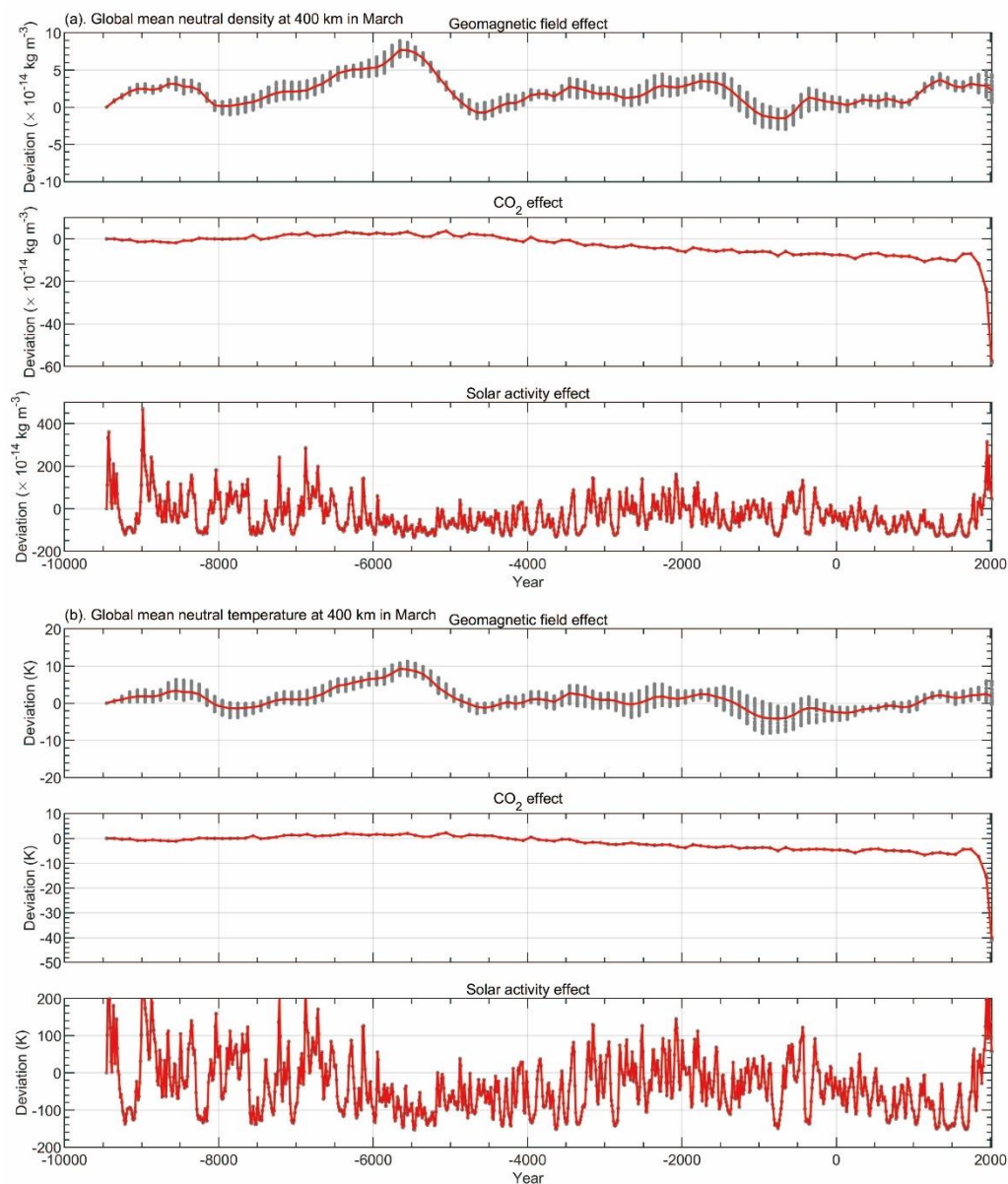


Figure 5: Global mean (red line) neutral density (a) and temperature (b) deviations with respect to the beginning of the simulation versus years at 400 km during the March equinox due to the geomagnetic field variation (CR1), the CO₂ variation (CR2), and the solar activity variation (CR4–CR3). The grey dots represent different UT results.

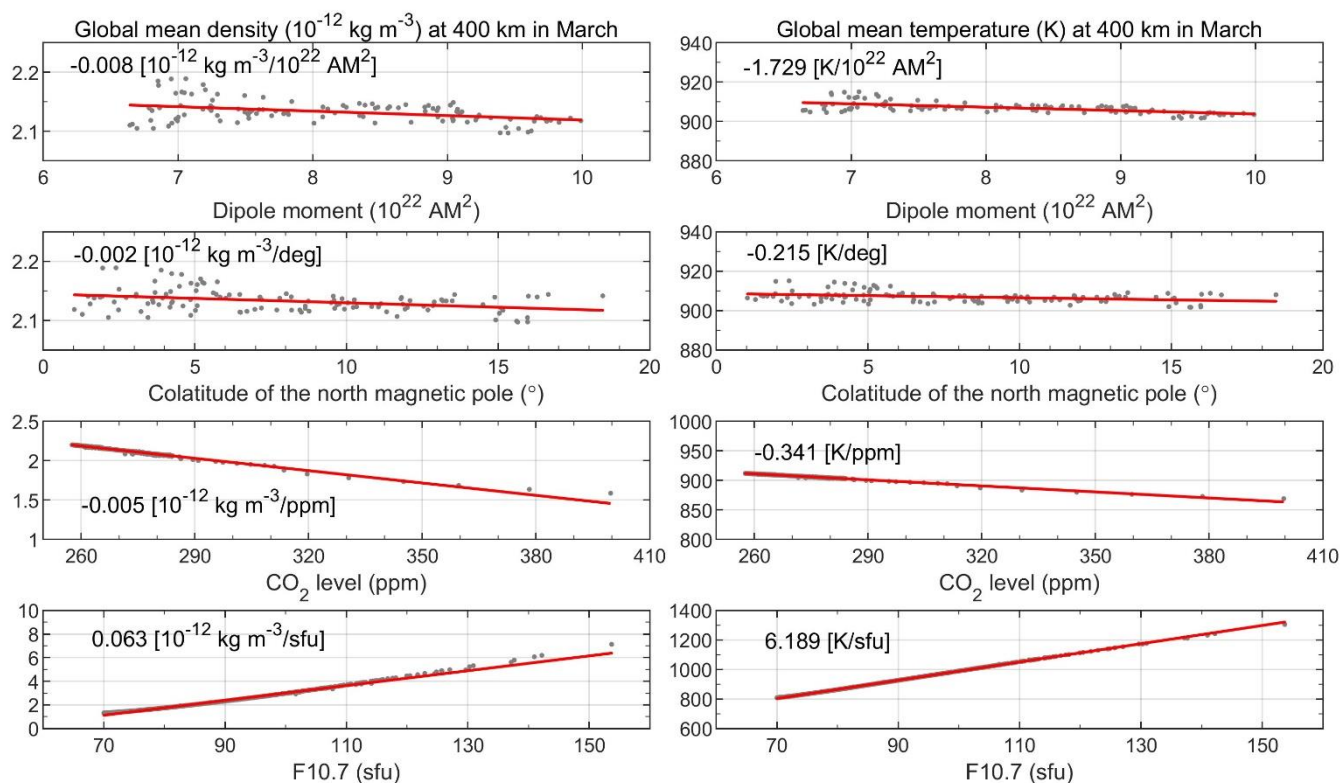


Figure 6: Simulated global mean neutral density (left column) and temperature (right column) at 400 km versus the geomagnetic field dipole moment (top row, CR1), the colatitude of the north magnetic pole (second row, CR1), the CO_2 level (third row, CR2), and the F10.7 index (bottom row, CR4–CR3) in the March equinox. The red line is the corresponding linear fitting results and the number in each panel is the corresponding fitted linear growth rate.

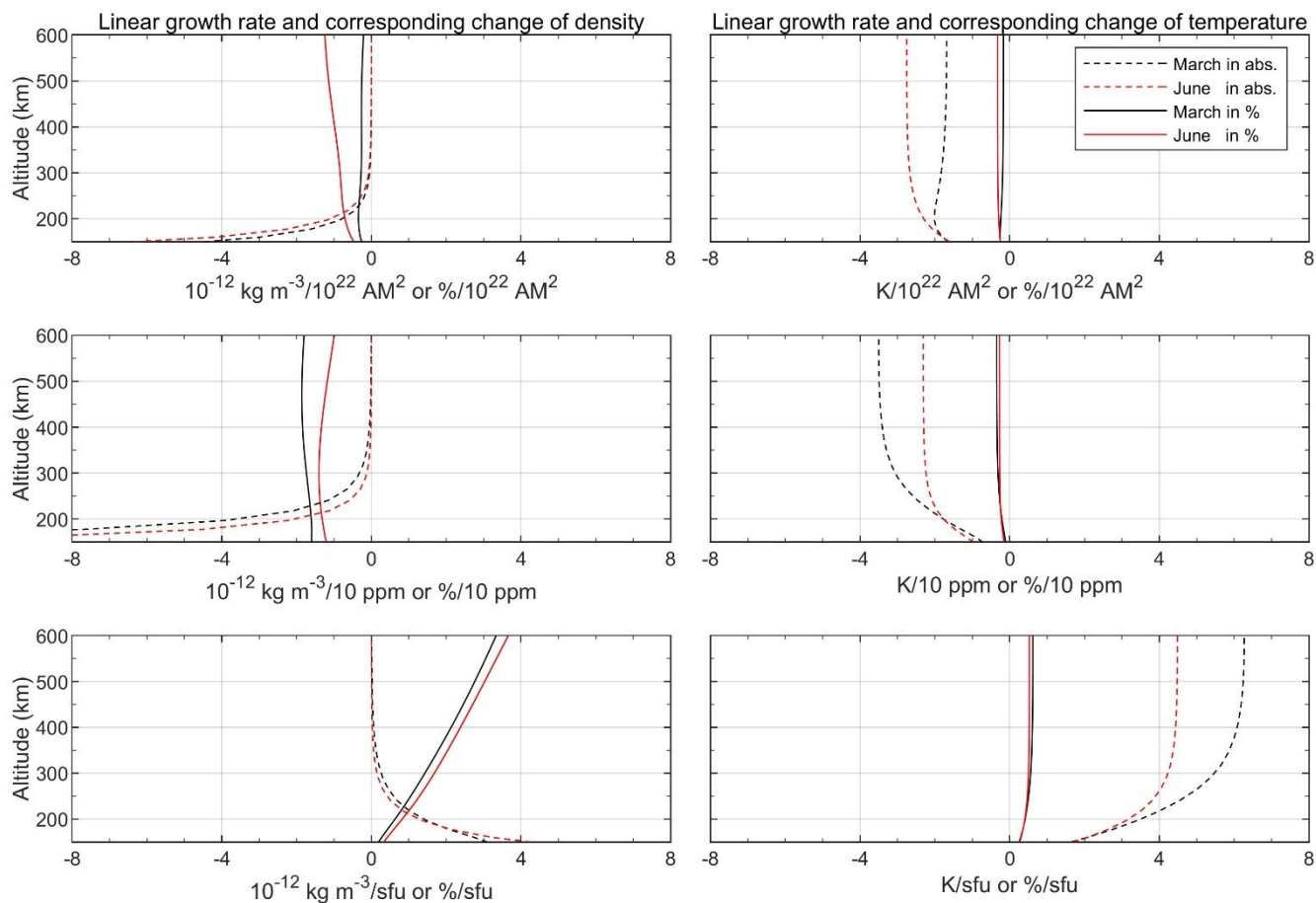


Figure 7: The altitude variations of the linear growth rate (dashed lines) and the corresponding change in percentage (solid lines) of global mean neutral density (left column) and temperature (right column) resulting from the dipole moment (top row, 485 CR1), the CO₂ level (middle row, CR2), and the F10.7 index (bottom row, CR4–CR3) in the March equinox (black lines) and June solstice (red lines).

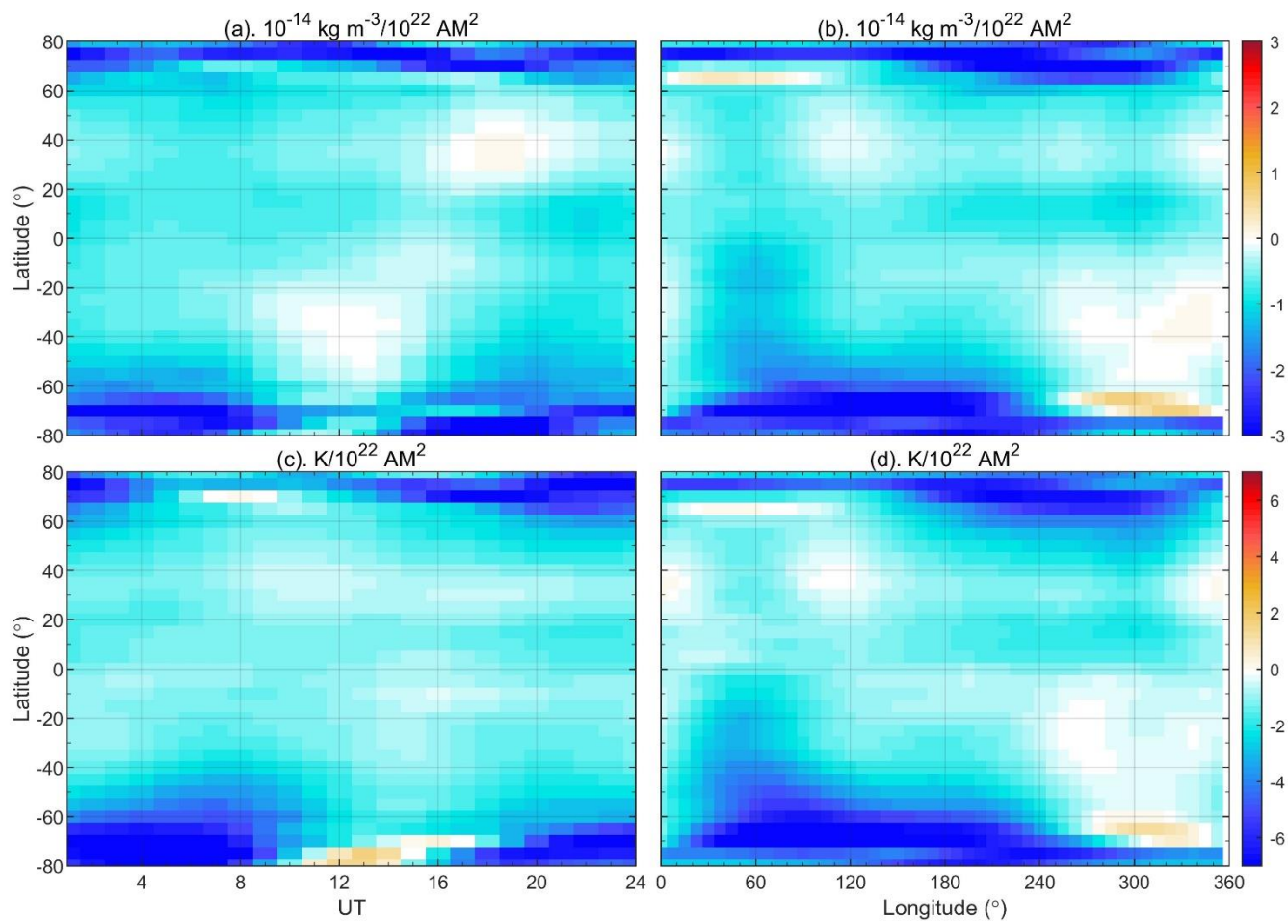


Figure 8: The latitude and longitude variations of the linear growth rate of neutral density (b) and temperature (d) due to the geomagnetic field. Panels (a) and (c) are the corresponding linear growth rate of zonal mean neutral density and temperature versus latitude and UT.